ACS APPLIED MATERIALS & INTERFACES

Research Article

www.acsami.org

Enhancing the Performance of Solution-Processed Bulk-Heterojunction Solar Cells Using Hydrogen-Bonding-Induced Self-Organization of Small Molecules

Kwan Hang Lam,[†,‡] Thelese Ru Bao Foong,[‡] Zi En Ooi,[‡] Jie Zhang,[‡] Andrew Clive Grimsdale,[†] and Yeng Ming Lam*[,†,§,∇]

[†]School of Materials Science and Engineering, Nanyang Technological University, Blk N4.1, Nanyang Avenue, Singapore 639798

[‡]Institute of Materials Research and Engineering (IMRE), Agency for Science Technology and Research (A*STAR), 3 Research Link, Singapore 117602

[§]Energy Research Institute @ NTU (ERI@N), Nanyang Technological University, 50 Nanyang Drive, Singapore 637533

[∇]Institute of Materials for Electronic Engineering II, RWTH-Aachen, Sommerfeldstraße 24, D-52074 Aachen, Germany

Supporting Information

ABSTRACT: Small-molecule solar-cell performance is highly sensitive to the crystallinity and intermolecular connectivity of the molecules. In order to enhance the crystallinity for the solution-processed small molecule, it is possible to make use of carboxylic acid end-functional groups to drive hydrogen-bonding-induced $\pi-\pi$ stacking of conjugated molecules. Herein, we report the synthesis and characterization of quarterthiophenes with carboxylic acid as end groups. The formation of hydrogen bonds between neighboring acid groups gives rise to a pseudo-polymeric structure in the molecules, which leads to substantial improvement in the organization and crystallinity of the active layers. This resulted in a four-fold increase in the hole mobility and a two-fold improvement in the performance of the solar cell device for the acid-functionalized molecule, compared to its ester analogue. More importantly, optimal device performance for the acid-functionalized molecule was achieved for the as-cast film, thereby reducing the reliance on thermal annealing and solvent additives.

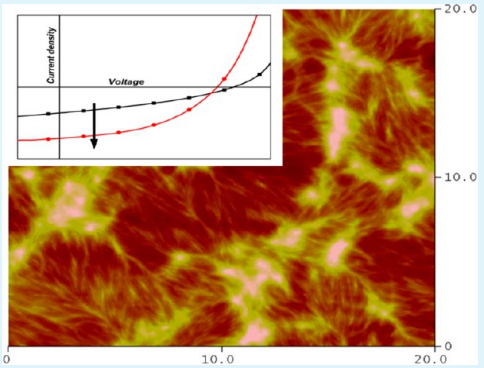

KEYWORDS: *small-molecule organic solar cells, solution processable, self-assembly, hydrogen bonding, quarterthiophene, carboxylic acid*

1. INTRODUCTION

Research into new materials for organic photovoltaics (OPVs) have focused mainly on polymeric semiconductors, because of their good film-forming properties, high charge carrier mobility, and device performance.[1−6] The bulk-heterojunction (BHJ) device architecture remains ubiquitous, as it gives rise to large interfacial area between the donor and acceptor phases, which leads to higher exciton splitting efficiency and, therefore, an increase in charge generation.[7−11] However, synthesis of semiconducting polymers has been plagued by issues such as batch-to-batch reproducibility, difficulty in purification, and high polydispersity in molecular weight. Hence, there has been growing interest in using small molecules as an alternative class of active donor materials for OPVs.

In contrast to polymers, small molecules are generally easier to purify and its molecular weight is monodispersed in nature. However, the device performance of solution-processed small-molecule-based OPVs generally has been lagging behind that of its polymeric counterpart. Although with increased effort invested device efficiencies have improved,[2,12−16] the issue of poor connectivity between the molecules has not been properly addressed. This lack in intermolecular connectivity will lead to lowered charge carrier mobility and device performance. For polymeric systems, it is well-established that high molecular weight (M_W) are crucial for good solar-cell performance.[17−20] This is due to the improved interchain connectivity and enhanced charge mobility along the polymer chains. These same requirements also apply to small-molecule systems. Lee et al. recently re-emphasized the importance of interconnectivity between small molecules by showing that pyrene, when attached at an appropriate carbon position, can facilitate the self-assembly and interconnectivity of small molecules, thereby improving solar-cell performance.[21] It is believed that, by incorporating hydrogen bonding into solution-processable small molecules, a similar effect can be achieved. The hydrogen-bond-induced $\pi-\pi$ interaction can lead to enhance

Received: September 28, 2013
Accepted: November 11, 2013
Published: November 11, 2013

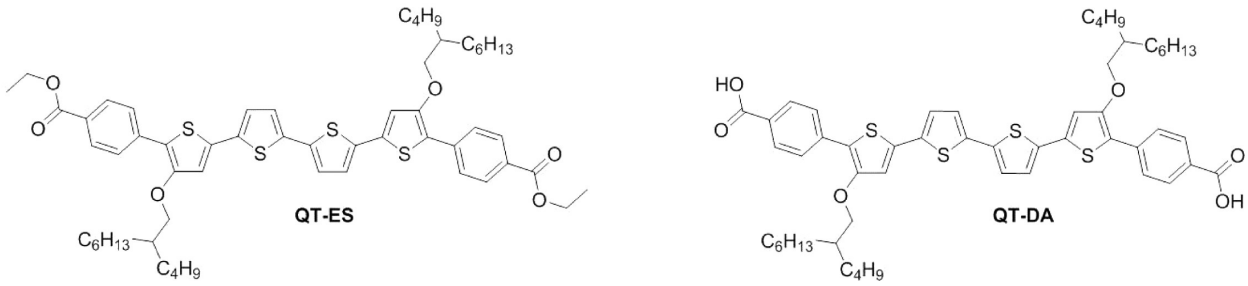

Figure 1. Chemical structures of quarterthiophene with diester groups (QT-ES) and quarterthiophene with diacid groups (QT-DA).

intermolecular connectivity and crystallinity. Wasserfallen et al. have previously reported on the functionalization of hexa-perihexabenzocoronene (HBC) with monocarboxylic and dicarboxylic acids, with the focus being placed on the effect of hydrogen bonding on the distinct columnar packing of HBCs.[22] However, the effect of the packing on solar cell performances was not reported.

Herein, we report the use of carboxylic acid end-functional groups, together with a conjugated core of quarterthiophene, abbreviated as QT-DA (shown in Figure 1), as a proof of concept. The positioning of the −COOH groups in QT-DA can result in the formation of a pseudo-polymer during the spin-coating process, thereby imparting good intermolecular connectivity, similar to that of polymers. This improved connectivity and crystallinity resulted in a higher hole mobility and an improvement in solar cell efficiency by more than two-fold for QT-DA, compared to its diester analogue (QT-ES, shown in Figure 1). Nanofibers were observed for the first time in solution-processed small-molecule active layers (QT-DA system), and this is a strong indication that, with the presence of carboxylic acid end-functional groups, there is a higher propensity for crystallization. Furthermore, thermal treatment was not necessary to achieve optimal device performance for the QT-DA system, because of the presence of hydrogen-bond-induced $\pi-\pi$ interaction.

2. EXPERIMENTAL SECTION

Details for the synthesis of the molecules are provided in the Supporting Information. All solvents were purchased in anhydrous grade from Sigma−Aldrich. Tetrakis(triphenylphosphine)palladium (0) ($Pd(PPh_3)_4$) was purchased from Strem Chemicals. All other chemicals were purchased and used without further purification.

^{1}H NMR and ^{13}C NMR spectra were collected using a Bruker DPX 400 MHz spectrometer. Chemical shifts are given in ppm downfield, with respect to tetramethylsilane. ultraviolet−visible (UV-vis) spectra were recorded using a Shimadzu Model 2501-PC system. Fourier transform infrared spectroscopy (FTIR) was performed on KBr disks with a Perkin−Elmer Spectrum GX device. Matrix-assisted laser desorption ionization time-of-flight (MALDI-TOF) measurements was conducted on a Shimadzu Biotech AXIMA Performance system, with Ditranol as the matrix. Thermogravimetric analysis (TGA) was conducted with TA Instruments Model HI-Res TGA 2950 system, using a heating rate of 10 °C/min. Differential scanning calorimetry (DSC) was carried out under nitrogen environment in a TA Instrument DSC Q100 equipment with a heating rate of 10 °C/min. The highest occupied molecular orbital (HOMO) levels for the molecules were measured with photoelectron yield spectroscopy in air (PESA) using a Riken Kekei AC-2 spectrometer.

Solar cells were fabricated on indium tin oxide (ITO)-coated glass with an average sheet resistance of 14 Ω/□. The ITO/glass substrates were cleaned in Hellmanex solution (10 min), deionized water twice (10 min each), acetone (15 min), and isopropanol (15 min), and then subsequently dried with pressurized nitrogen. The dried substrates were then subjected to UV-ozone cleaning for 10 min at 100 °C prior to the spin coating of a 40-nm-thick poly(3,4-ethylenedioxythiophene):poly(styrenesulfonate) (PEDOT:PSS) (CLEVIOS P VP Al 4083, H.C. Starck) hole transporting layer. Annealing of the PEDOT:PSS layer was done in a nitrogen-filled glove box at 140 °C for 10 min. Subsequently, blends of the active materials were spin-coated on top of the PEDOT:PSS layer in the glove box. Cathode layers (aluminum with thicknesses of ∼80 nm) were evaporated through a shadow mask at a pressure of $<6 \times 10^{-6}$ mbar to obtain devices with an active area of 9 mm^2. The blend solutions for QT-ES were prepared by dissolving the donor molecules and $PC_{61}BM$ simultaneously in chloroform or chlorobenzene heated to 50 °C and stirred overnight. For the blend solutions of QT-DA, the donor molecules were first dissolved in a 1:1 volume ratio of THF and DMF and stirred at 50 °C for 2 h. The $PC_{61}BM$ were dissolved separately in *o*-dichlorobenzene at 50 °C for 2 h, after which the $PC_{61}BM$ solution was added into the donor solution kept at 50 °C and stirred overnight. Current density−voltage ($J-V$) characteristics for solar cell devices were measured with a Keithley Mode SMU 2400 sourcemeter under AM1.5G illumination from a solar simulator with a calibrated power intensity of 100 mW/cm^2. The external quantum efficiency (EQE) was measured with a mechanically chopped (213 Hz) monochromatic light from a 300-W Xe lamp. A Stanford Research Systems Model 830 lock-in amplifier was used to detect the spectrally resolved photocurrent via a voltage signal by passing the current through a 50 Ω resistor. All measurements were taken in a glove box under nitrogen environment.

Hole mobility devices were measured with the space-charge limited current (SCLC) method with a hole-only device. The device configuration was ITO/PEDOT:PSS/active layer/MoO_3/Al and mobilities were determined by fitting the dark current curve with a field-dependent mobility equation, given as

$$J = \left(\frac{9}{8}\right)\varepsilon_0\varepsilon_r\mu_h\left(\frac{V_{eff}^{\ 2}}{L^3}\right)$$

where J is the current density, μ_h the hole mobility, ε_0 the permittivity of free space, ε_r the relative permittivity of the materials (assumed to be 3, which is typical of organic semiconducting materials), L the film thickness, and V_{eff} the effective voltage. The effective voltage is obtained by subtracting the applied voltage with the built-in voltage and the voltage drop from the series resistance in the device. The built-in voltage was estimated from the open-circuit voltage of illuminated hole-only devices.[23−25]

Film thickness was measured using a KLA Tencor P-10 step profiler, while atomic force microscopy (AFM) images were collected with a Digital Instruments Nanoscope IIIa system in tapping mode. X-ray diffraction (XRD) patterns were collected using the Bruker General Area Detector Diffraction System (GADDs) with Cu Kα radiation equipped with a 2D detector. Scans were taken over a 2θ range of 2°−30° with a scan duration of 10 min (incident X-ray at 2°).

3. RESULTS AND DISCUSSION

3.1. Synthesis and Material Characterization. The chemical structures of the ester and acid end-functionalized small molecules are shown in Figure 1 and are abbreviated as

Scheme 1. Synthetic Route for QT-ES and QT-DA

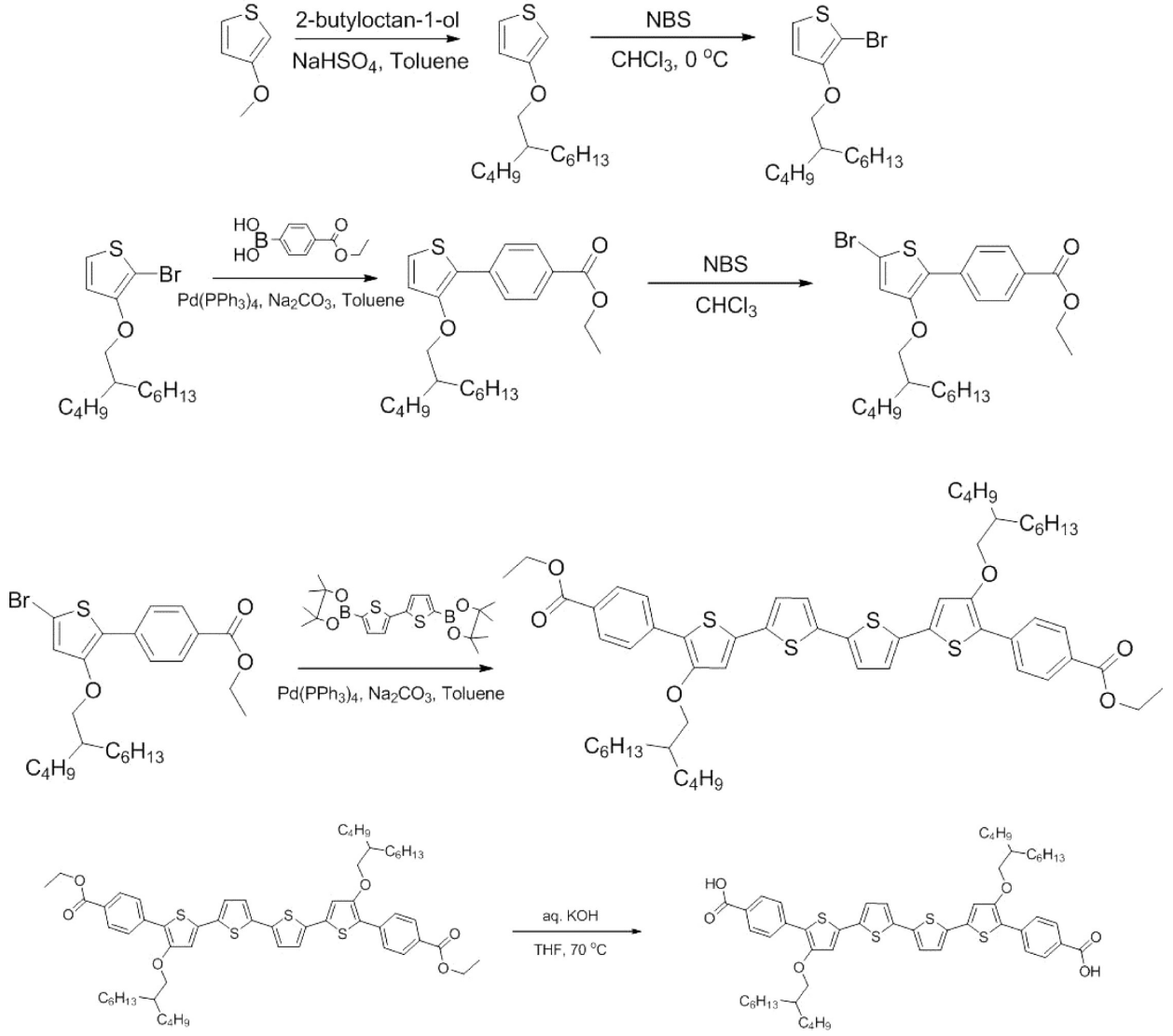

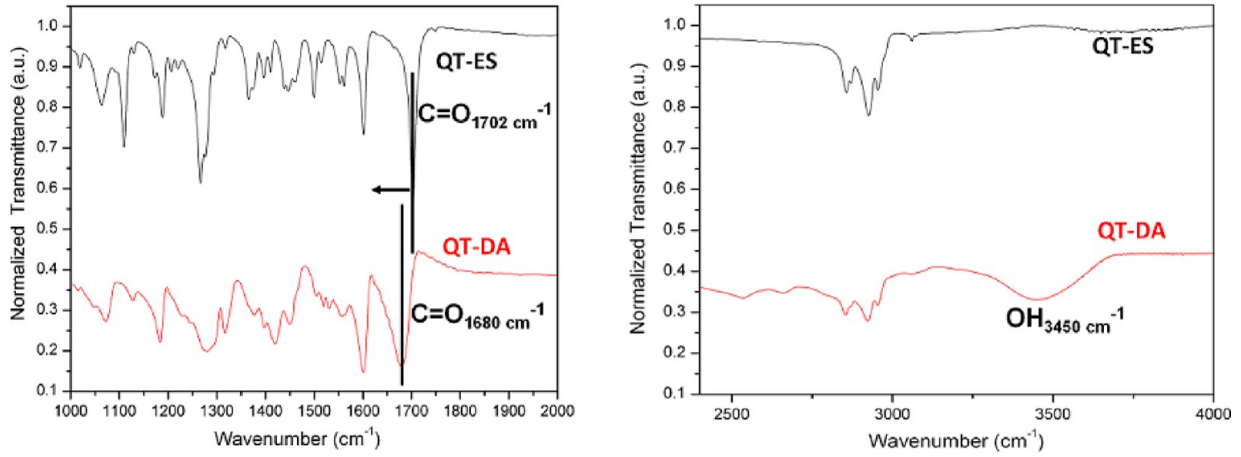

Figure 2. Fourier transform infrared (FTIR) graph of QT-ES and QT-DA for the 1000−2000 cm^{-1} range (left) and for the 2500−4000 cm^{-1} range (right).

QT-ES and QT-DA, respectively. Branched alkoxy solubilizing chains were chosen since the flexibility provided by the ether bonds, together with the branched units, can contribute to the enhanced solubility of small molecules, compared to linear alkyl chains.[26−28] Another additional advantage of using the alkoxy group is its electron-donating nature; hence, it is predicted that

a certain degree of intramolecular donor−acceptor interaction between the side chain and the electron-withdrawing group (carboxylic acid) will be present. The substitution of −COOH groups at the α- and ω-positions of QT-DA will result in the formation of a pseudo-polymer through hydrogen bonding. This design essentially provides the advantage of small molecules (ease of synthesis and reproducibility) and polymers (good intermolecular connectivity) simultaneously.

Scheme 1 shows the synthetic route for QT-ES and QT-DA. The first step of the synthesis involved a nucleophilic substitution of 3-methoxythiophene with 2-butyloctanol, after which the product was brominated with *N*-bromosuccinimide (NBS), followed by coupling with 4-(ethoxycarbonyl)phenyl boronic acid via Suzuki coupling. Subsequently, the product was brominated again and coupled with 2,2′-bithiophene-5,5′-diboronic acid bis(pinacol) ester resulting in the donor molecule, QT-ES. To obtain QT-DA, the hydrolysis of QT-ES by potassium hydroxide was performed, followed by acidification with aqueous hydrochloric acid. Purification of QT-DA was achieved with column chromatography followed by recrystallization from THF/hexane. It is interesting to note that attempts to couple 2-bromo-3-(2-butyloctyloxy)thiophene with 2,2′-bithiophene-5,5′-diboronic acid bis(pinacol) ester were unsuccessful. Instead, homo-coupling of butyloctyloxy thiophene dimers, trimers, and oligomers tended to occur. This was postulated to be related to the possibility of halogen-boron exchange in 2-bromo-3-(2-butyloctyloxy)thiophene resulting in the homo-coupling of alkoxythiophenes.

FTIR scans in Figure 2 show a red-shifting of ∼20 cm^{-1} in the carbonyl peak (C═O) from 1702 cm^{-1} (for QT-ES) to 1680 cm^{-1} (for QT-DA). This shift was due to a difference in the stabilization of the resonance structures and the presence of hydrogen bonding in carboxylic acid groups.[29,30] The appearance of the 3450 cm^{-1} peak can be attributed to the presence of hydroxyl (OH) groups in QT-DA and provided further evidence indicating the successful hydrolysis of the ester group to carboxylic acid. The broad OH peak centered at 3450 cm^{-1}, as opposed to a sharp peak between 3600 cm^{-1} and 3700 cm^{-1} for free hydroxyl groups, was an indication that QT-DA molecules existed in the oligomeric form because of hydrogen bonding.[31] From the ^{1}H NMR spectra of QT-DA (see Figure S1b in the Supporting Information), the disappearance of the quartet protons at 4.39 ppm, together with the appearance of a proton signal at ∼11 ppm, indicates the successful conversion of ester to an acid functional group. The m/z values of 995.4467 and 939.3854, obtained from high-resolution mass spectrometry, were similar to the calculated values of QT-ES (995.4441) and QT-DA (939.3815) respectively, which confirmed the molecular structure of the target molecules (see Figures S2 and S3 in the Supporting Information).

3.2. Thermal Properties. The decomposition temperature (T_d) of the molecules was measured using thermogravimetric analysis (TGA) and was found to exceed 350 °C, indicating a relatively high thermal stability, which is beneficial for both device fabrication and operation (see Figure S4 in the Supporting Information). From the differential scanning calorimetry (DSC) measurement, both molecules showed a single melting (T_M) and crystallization (T_C) peak with no signs of a glass-transition temperature (T_g). Looking at Figure 3, it can be observed that both the T_M and T_C values of QT-DA showed an increase of at least 200 °C, compared to those of QT-ES. A summary of the thermal properties for both molecules is shown in Table 1. The increase in the thermal

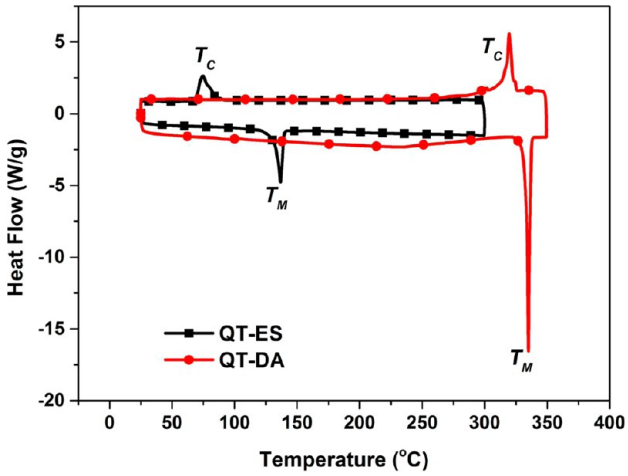

Figure 3. Differential scanning calorimetry (DSC) of QT-ES and QT-DA with the melting temperature (T_M) and crystallization temperature (T_C) labeled.

Table 1. Summary of Thermal Properties of QT-ES and QT-DA

sample	T_d (°C)	T_M (°C)	T_C (°C)	ΔH_{fus} (J/g)[a]
QT-ES	389	132.28	74.70	53.25
QT-DA	362	333.02	319.80	95.35

[a]Enthalpy of fusion from DSC measurements.

transition temperatures is an indication of an enhanced intermolecular connectivity and crystallinity in QT-DA, which is attributed to the presence of hydrogen-bonding-induced $\pi-\pi$ stacking. On the other hand, since only $\pi-\pi$ interaction between neighboring QT-ES molecules can occur, this limits its intermolecular interaction strength and, thus, the connectivity between the molecules and the film crystallinity. This difference in film crystallinity is particularly important for solution-processed OPVs, as this will have a direct impact on the charge mobility and device performance. Solvent additives or annealing at elevated temperature or by using solvent vapor is usually required for solution-processed devices to achieve the optimum crystallinity and device efficiencies.[5,8,32,33] Hence, our objective of introducing −COOH moieties into the molecular structure was to achieve high intermolecular connectivity, which can lead to optimum morphology without additional treatment.

3.3. Optical Properties and Energy Levels. The optical absorption of both molecules in solution and thin film were investigated using UV-vis spectroscopy and are shown in Figure 4a. The solution-phase absorption was performed in chloroform for QT-ES and in THF for QT-DA (because of the difference in solubility for both molecules) at a concentration of 10^{-5} M to eliminate the presence of aggregates and it was observed that both QT molecules have very similar absorption profile. A red-shift in the absorption onset for thin films, compared to the solution phase of the molecules, was observed and can be attributed to the formation of J-aggregates, leading to an increase in the mixing of the intermolecular orbitals.[34,35] Interestingly, the red-shifting in the onset of thin film absorption was more pronounced for QT-DA, compared to QT-ES. In fact, the extent of the red-shift is a good indication of the extent of the $\pi-\pi$ interaction present in QT-DA, compared to QT-ES. Because of the presence of hydrogen-bond-induced

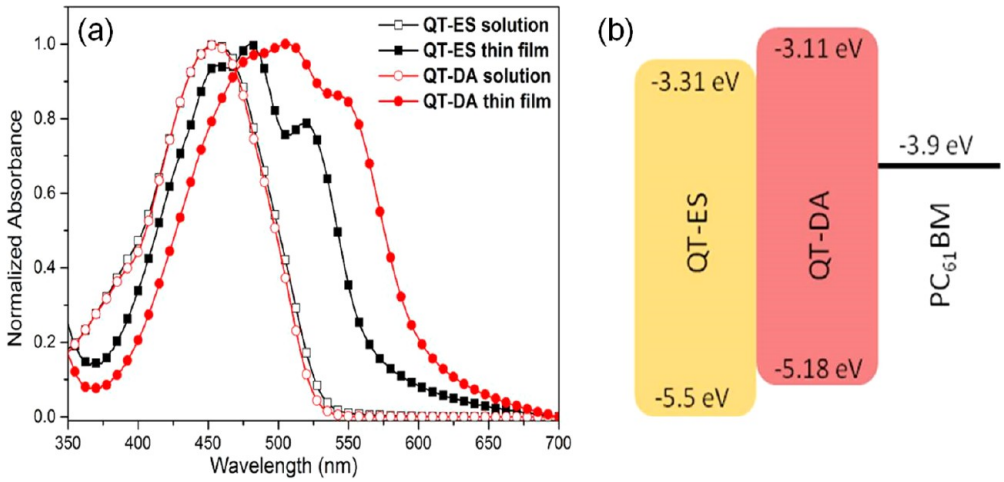

Figure 4. (a) Normalized ultraviolet−visible (UV-vis) absorption of QT-ES (in chloroform) and QT-DA (in THF) in solution and for thin films. (b) Energy diagram for QT donor molecules and $PC_{61}BM$.

$\pi-\pi$ stacking, the red-shift of QT-DA thin film absorption is higher. This observation is consistent with the higher thermal transition temperatures observed for QT-DA.

The energy levels of the molecules are important as this determine the choice of the acceptors that can be used. A schematic diagram for the energy levels of both QT molecules and $PC_{61}BM$ is shown in Figure 4b. The highest occupied molecular orbital (HOMO) levels of the donor molecules were determined using photoelectron yield spectroscopy in air (PESA) (see Figure S5 in the Supporting Information). The measurements were carried out on thin films giving the closest representation of the devices. The lowest unoccupied molecular orbital (LUMO) levels were calculated from the optical bandgap (E_g^{opt}) and HOMO levels. It was observed that the bandgap of QT-DA is 0.12 eV lower compared to QT-ES. A summary of the optical properties and energy levels for QT-ES and QT-DA are listed in Table 2.

Table 2. Summary of Optical Properties and Energy Levels of QT-ES and QT-DA

	λ_{max} (nm)				
sample	solution[a]	film	HOMO (eV)	LUMO (eV)	E_g^{opt} (eV) (film)
QT-ES	457	480	−5.50	−3.31	2.19
QT-DA	456	506	−5.18	−3.11	2.07

[a]Solution UV-vis absorption for QT-ES and QT-DA are done in chloroform and THF, respectively.

3.4. Solar Cell Fabrication and Characterization. BHJ solar cells were fabricated using solution-deposited QT molecules as the donor and $PC_{61}BM$ as the acceptor; an optimized donor-to-acceptor ratio of 1:1 was used for this study. The device structure employed was ITO/PEDOT:PSS/active layer/Al, whereby the aluminium cathode was deposited by thermal evaporation. QT-ES is readily soluble in common chlorinated solvents such as chloroform and chlorobenzene; hence, it was dissolved concurrently with $PC_{61}BM$. Since QT-DA is not soluble in chlorinated solvents, a solvent mixture of THF and DMF (1:1 by volume) was used as the processing solvent. A THF:DMF mixture was used because DMF, while being a good solvent, has a boiling point that is too high, resulting in films with pinholes, which will lead to device shorting. THF was added to counteract this problem, giving rise to better solubility and processability.

The active layer thickness was kept at ∼80 nm, since this thickness gave the most efficient device performance. Thickness variation was achieved by varying the spin-coating speed while keeping the blend concentration constant. Devices with thicker active layers (120−150 nm) resulted in cells of lower efficiency, mainly because of a lower short circuit current density (J_{sc}) (see Figure S7 and Table S1 in the Supporting Information). This was due to a relatively low hole mobility of the QT molecules, which will be shown later. For a thick active layer, effective charge transportation becomes more crucial and low mobility can lead to poor charge transportion and a reduction in J_{sc}.[36] On the other hand, devices with thickness below 60 nm were often leaky and resulted in cells shorting.

The current density−voltage ($J-V$) characteristics and external quantum efficiency (EQE) of the optimized devices are shown in Figure 5. The QT-ES:$PC_{61}BM$ devices fabricated using chloroform as the solvent performed poorly prior to thermal annealing, and upon heating at 70 °C for 10 min, the power conversion efficiency (PCE) improved by ∼20-fold, to 0.39% (from Table 3). The use of heat treatment is a common practice to encourage phase separation and crystallization in the active layer of both polymeric[8,37,38] and small-molecule[39−41] BHJ OPVs. An optimal phase separation of the donor and acceptor phases will create hole and electron transport channels for easier charge transport to their respective electrodes. Upon spin-coating of the QT-ES:$PC_{61}BM$ blend solution, both phases were intimately mixed, which resulted in hole or electron channels that were either discontinuous or too narrow for efficient charge transport.[42] During thermal annealing, molecular rearrangement can take place, leading to the crystallization of QT-ES. This crystallization, in turn, forces the $PC_{61}BM$ out from the donor phase, resulting in the formation of donor-rich and acceptor-rich phases. This phase separation would then provide the pathways for holes and electrons to travel to the electrodes, resulting in an increase in J_{sc} (from 0.22 mA/cm^2 to 1.44 mA/cm^2) and open circuit voltage (V_{oc}) (from 0.36 V to 0.78 V). Because of the low boiling point of chloroform (60 °C), the drying of the blend film will be extremely fast and hence there might be insufficient time for the crystallization to occur. Solvents with relatively higher boiling points, such as chlorobenzene (132 °C) and *o*-

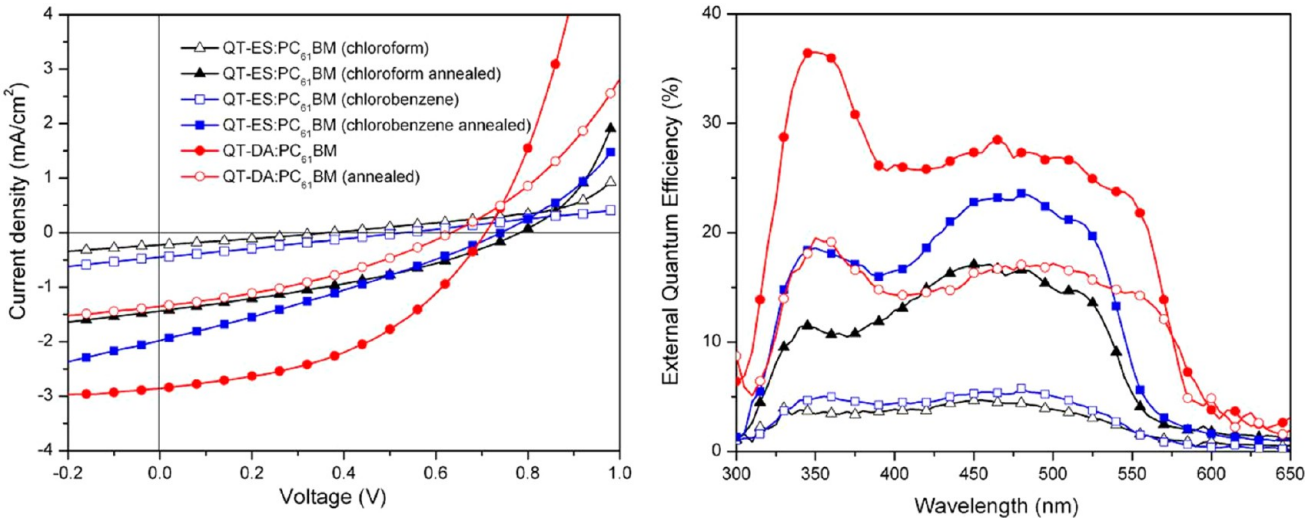

Figure 5. Current density–voltage (J–V) characteristics (left) and EQE spectra (right) of QT-ES:PC61BM and QT-DA:PC61BM devices.

Table 3. Photovoltaic Characteristics of Devices with Device Structure ITO/PEDOT:PSS/Donor:$PC_{61}BM$ (1:1 in wt %)/Al

sample	open-circuit voltage, V_{oc} (V)	short circuit current density, J_{sc} (mA/cm^2)	fill factor, FF (%)	power conversion efficiency, PCE (%)	Resistance (Ω cm^2)[a] series, R_s	Resistance (Ω cm^2)[a] shunt, R_{sh}
QT-ES:$PC_{61}BM$[b]						
non-annealed	0.36	0.22	27	0.02	1428	2000
annealed	0.78	1.44	34	0.39	244	909
QT-ES:$PC_{61}BM$[c]						
non-annealed	0.53	0.45	26	0.06	1111	1429
annealed	0.74	1.98	29	0.42	250	455
QT-DA:$PC_{61}BM$[d]						
non-annealed	**0.71**	**2.86**	**45**	**0.91**	**79**	**1250**
annealed	0.63	1.35	35	0.30	244	1000

[a] R_s and R_{sh} were calculated from the inverse slope of illuminated curves under open-circuit conditions and short-circuit, respectively. [b] Device fabricated from chloroform. [c] Device fabricated form chlorobenzene. [d] Device fabricated from THF/DMF.

dichlorobezene (178 °C), were then used to improve the phase separation between the donor and acceptor. The drying of these solvents will be slower, compared to that of chloroform, thereby providing a longer time for the QT-ES molecules to form more ordered and larger donor and acceptor phases for holes and electrons extraction. From Table 3, devices as cast from chlorobenzene showed slightly better performance, compared to that from chloroform; however, these devices still required similar heat treatment to attain the optimum device performance. This is because, inherently, QT-ES has a low tendency to crystallize and the presence of $PC_{61}BM$ further disrupts the molecular ordering. Hence, even with chlorobenzene, there is insufficient time for the formation of appropriately sized donor and acceptor phases. It was found that further annealing beyond 10 min resulted in the degradation of QT-ES device performances, most probably due to excessive phase separation and, hence, reduction in interfaces for excitons to split.[43] Devices processed from *o*-dichlorobezene gave much lower efficiencies, compared to chloroform and chlorobenzene (see Figure S8 in the Supporting Information) which was attributed to a much lower solubility of QT-ES in the solvent. In general, the fill factor (FF) of the QT-ES:$PC_{61}BM$ devices was relatively low (~30 %), which could be due to the poor mobility of QT-ES, resulting in unbalanced charge transport in the devices. An interesting point to note was the difference in the J–V characteristics of the annealed QT-ES devices that were processed with chloroform and chlorobenzene. Although the PCE of devices fabricated using the two processing solvents were similar, we observed that the annealed films from chloroform had a lower J_{sc} value and higher V_{oc} value, compared to chlorobenzene. This is related to the film morphology, as can be seen from the atomic force microscopy (AFM) images shown later in Figure 7. Looking at Figures 7a and 7b, the domain size of the active layer prepared using chlorobenzene was smaller compared to that processed using chloroform. This was evident from the root-mean-square (r.m.s) roughness values of 3.07 nm for chlorobenzene and 3.58 nm for chloroform, indicating a smoother film from the former. The smaller domain size obtained from chlorobenzene-processed films could be attributed to a higher solubility of QT-ES in the solvent. It was found that QT-ES has a slightly higher solubility in chlorobenzene (40 mg/mL), compared to that in chloroform (30 mg/mL). The reduced domain sizes provided a larger surface area between the donor and acceptor phases, which would translate to a higher density of exciton splitting and charge generation rate. This was observed in the higher J_{sc} value of chlorobenzene, compared to chloroform-processed films. However, an increase in surface area could result in a higher tendency for recombination between the electron–hole

pairs during charge transportation. Shunt resistance (R_{sh}) has been related to the recombination of charge carriers near the donor−acceptor interfaces or near the electrode interfaces.[44,45] It can be seen from Table 2 that there was indeed a decrease in the R_{sh} for devices processed with chlorobenzene (455 Ω cm^2), with respect to chloroform (909 Ω cm^2), which indicated an increase in recombination for the former. This, in turn, was accompanied by a decrease in the V_{oc} value for chlorobenzene devices (0.74 V), compared to that for chloroform devices (0.78 V).[45,46]

Contrary to the QT-ES:$PC_{61}BM$ blends, annealed devices of QT-DA:$PC_{61}BM$ displayed a lower PCE, compared to as-cast ones (60% reduction in PCE). The most affected parameter was the J_{sc} value, which was decreased by ∼50% (from 2.86 mA/cm^2 to 1.35 mA/cm^2), while the V_{oc} value decreased from 0.71 V to 0.63 V for the annealed devices. AFM images (see Figures 7c and 7d, presented later in this work) showed that there was an increase in the root-mean-square (rms) roughness for the annealed films (16.84 nm), compared to as-cast films (14.42 nm). This was ascribed to the aggregation of QT-DA molecules, which resulted in the formation of large domains. This increase in roughness can result in poor interfacial contact between the active layer and the metal cathode, leading to an increase in the series resistance (R_s) from 79 Ω cm^2 to 244 Ω cm^2.[47] Therefore, the increased R_s value led to a decrease in the J_{sc} value of the annealed QT-DA:$PC_{61}BM$ devices. Furthermore, the aggregation of QT-DA may lead to a decrease in the interfacial area between donor and acceptor, thereby reducing the exciton separation and charge generation yield.[48,49] Various annealing temperatures, ranging from 70 °C to 120 °C, were studied, and similar results were observed. Therefore, it is believed that an optimum phase separation was achieved upon spin coating of the QT-DA:$PC_{61}BM$ blend solution and further annealing destroys this optimal separation.

Most importantly, it was observed that the PCE of optimized QT-DA:$PC_{61}BM$ devices was two-fold higher than that of QT-ES:$PC_{61}BM$. This improvement was mainly coming from much-higher J_{sc} and FF values achieved by the as-cast QT-DA:$PC_{61}BM$ devices. The improved FF value was due to a more-balanced electron and hole transport, because of an increase in the hole mobility of QT-DA. In order to verify the enhanced hole mobility of QT-DA, compared to QT-ES, space-charge limited current (SCLC) measurements were used to investigate the neat film hole mobilities. The SCLC method was employed because it measures the mobility perpendicular to the substrate plane and this is more representative of the solar-cell device configuration. Figure 6 shows a plot of the $J^{0.5}$ vs V_{eff} plot, and the hole mobilities of QT-DA and QT-ES were calculated to be 2.83 × 10^{-5} cm^2/(V s) and 6.91 × 10^{-6} cm^2/(V s) respectively. This showed that the hole mobility of QT-DA is four-fold higher than QT-ES, which can be attributed to an enhanced intermolecular connectivity and crystallinity in the QT-DA films. Such improvements in mobility of semiconducting molecules from an enhanced crystallinity have previously been reported.[50−52] Although it has been reported that the presence of acid groups can act as electron-trapping sites,[53] the presence of −COOH groups did not seem to have an effect on hole transportation. This was observed in this work and other published works related to polymers bearing carboxylic acid groups and small molecules bearing hydrogen-bonding groups.[54−57] Another important difference observed between the QT-DA and QT-ES devices was that annealing was not required to attain the optimum device performance for the former. Since no annealing was required to achieve the crystallinity, this would be beneficial for large-scale fabrication, because of reduced cost and time.

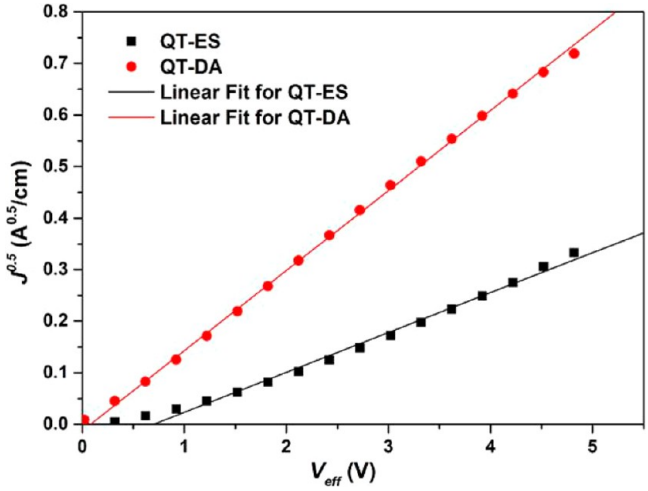

Figure 6. Graph of $J^{0.5}$ vs V_{eff} for hole-only devices of neat QT-ES and QT-DA films. Device configuration: ITO/PEDOT:PSS/neat film/MoO_3/Al with an active layer thickness of 70 nm.

3.5. Morphology of Blend Films. To further elucidate the effects of −COOH groups on the active layer morphology and their impact on solar-cell device performance, the topological information of the films were collected using AFM, and the images are shown in Figure 7. Considering the small difference in molecular design (i.e., acid versus ester end groups), the stark contrast in the morphology where the as-cast blend films of QT-DA showed the presence of nanofibers (Figure 7c), which were absent in QT-ES films, is remarkable. Such fibrous structures have previously been reported by our group[58,59] and others[60−62] for P3HT films, and they have been shown to result in better J_{sc} and device efficiency, because of improved hole mobility. These previous reports were mostly based on preformed nanofibers using poor solvent to encourage the crystallization followed by mixing with fullerenes to obtain the active blend solution. In this case, similar nanofiber formation was achieved for QT-DA:$PC_{61}BM$ devices through the molecular engineering of the donor small molecule where hydrogen-bond-induced $\pi-\pi$ interaction was leveraged. No signs of red-shifting in the QT-DA active blend solution were observed, which suggested that the fiber formation occurred during the spin-coating process. To the best of our knowledge, this is the first time that nanofiber formation is observed in solution-processed small-molecule solar cells. As mentioned previously, these fibers provided efficient charge transportation pathways, which were evident from the lowered R_s in QT-DA devices (79 Ω cm^2), with respect to QT-ES (244 Ω cm^2).

XRD patterns of the blend and neat films were carried out to elucidate the molecular ordering and confirm the enhanced crystallinity of QT-DA molecules. Figure 8a shows the diffraction pattern for annealed QT-ES:$PC_{61}BM$, while the inset shows that of the as-cast blend film. Prior to annealing, the crystallinity of the active layers was very weak, which corresponded to the poor device performances; however, upon annealing, we observed a (100) peak for QT-ES at 2θ = 3.8° which was calculated to correspond to d_{100}-spacing of 23.3 Å. The spacing can be ascribed to the distance between the conjugated backbones of the molecules separated by the branched alkyl chains. A similar distance was reported for

dx.doi.org/10.1021/am4042614 | ACS Appl. Mater. Interfaces 2013, 5, 13265−13274

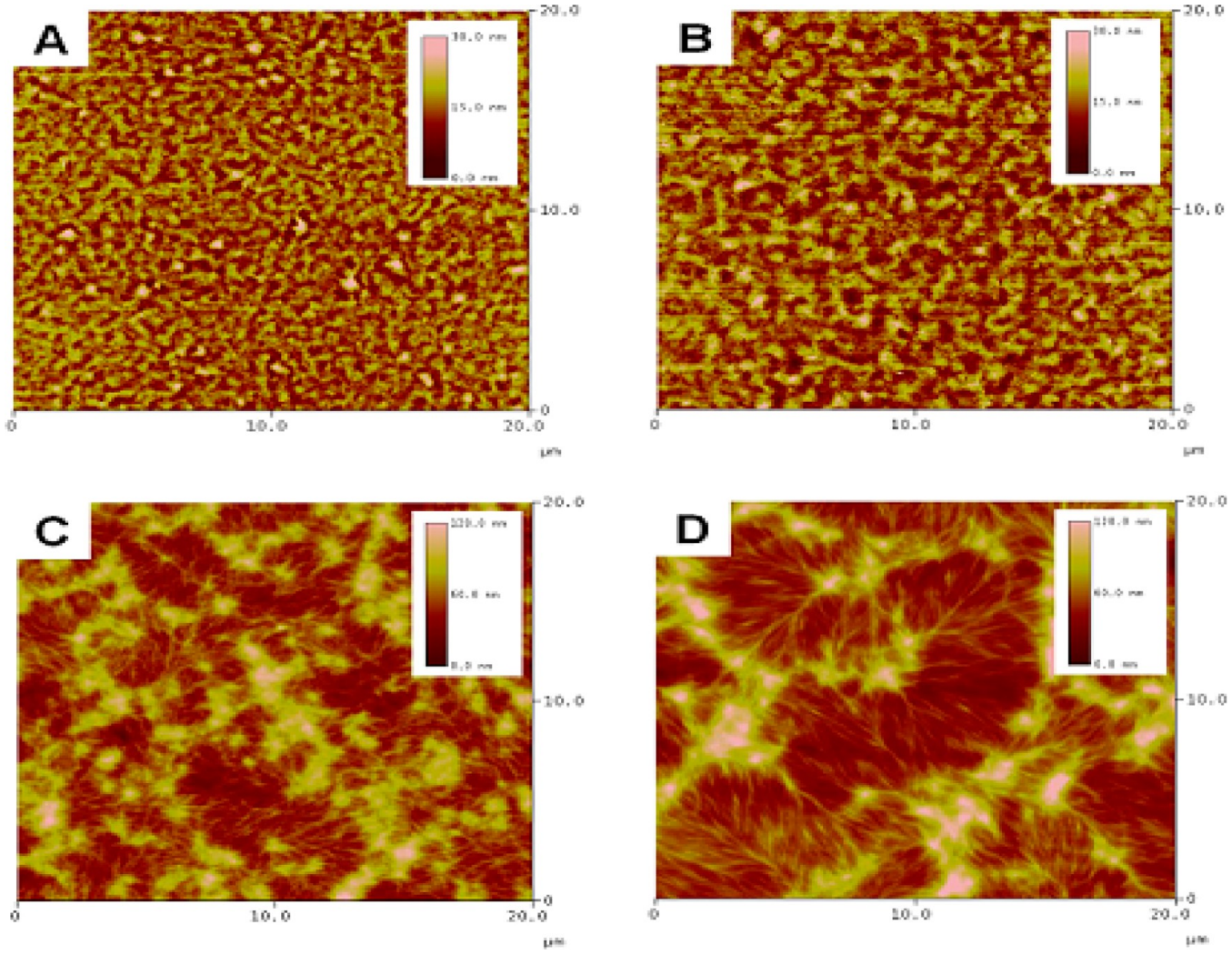

Figure 7. AFM tapping mode height images for annealed QT-ES:PC61BM devices spin-coated from (a) chlorobenzene and (b) chloroform, as well as for QT-DA:PC61BM devices spin-coated from THF/DMF ((c) as-cast and (d) annealed). Scale bars in panels (a) and (b) are 30 nm, while that bof (c) and (d) are 120 nm.

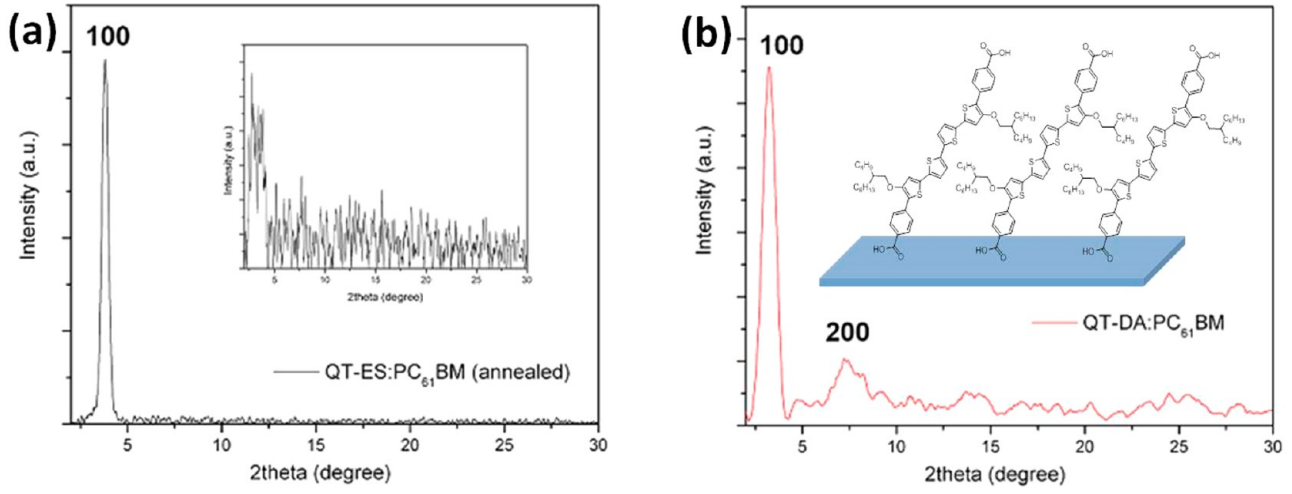

Figure 8. Integrated intensity diffraction pattern for films of (a) QT-ES:PC61BM and (b) QT-DA:PC61BM. The inset in panel (a) shows the non-annealed QT-ES:PC61BM film, while the inset in panel (b) shows the schematic diagram for the organization of QT-DA.

poly(3-octylthiophene-2,5-diyl) (P3OT), which has an alkyl chain length of eight carbon atoms (close to that of the donor molecules presented in this study).[63] Since only the (*h*00) peaks were seen from the XRD scans, it can be henceforth deduced that QT-ES adopted an edge-on configuration on the substrate, which was commonly seen for other semiconducting

molecules or polymers, especially P3HT.[64−66] On the other hand, from Figure 8b, diffraction peaks were clearly visible for the as-cast QT-DA active layers. This provided clear evidence for the enhanced crystallinity of QT-DA as compared to QT-ES. Furthermore, besides the first order peak, a weak signal attributed to the second order peak could be seen in the diffraction pattern of the as-cast blend film of QT-DA which signified a higher propensity for crystallization in QT-DA molecules. Therefore, annealing was not required for QT-DA:$PC_{61}BM$ films to achieve its good organization. The first-order peak for QT-DA corresponded to a *d*-spacing of 26.7 Å. The difference in the *d*-spacing values for QT-DA and QT-ES, despite having similar alkyl chains, was attributed to a difference in the molecular orientation. The length of QT-DA was calculated to be 27.9 Å (see inset of Figure 8b), and, hence, it is believed that QT-DA adopted a vertical alignment with a tilt angle of ∼73°, with respect to the substrate. The vertical alignment could be another reason for a higher hole mobility observed for neat films of QT-DA as the charge transportation will be more efficient along the backbone of the connecting molecules, compared to hopping through the conjugated backbones separated by alkyl chains.[67,68] Similar diffraction patterns were observed for the neat films (see Figure S9 in the Supporting Information).

Therefore, from the AFM images and XRD measurements, it can be seen that enhanced crystallinity and formation of nanofibers can be achieved in solution-processed small molecules by the introduction of −COOH groups at the α- and ω-position. This provides an improvement in the charge transport properties, which leads to an increase in the power coversion efficiency (PCE) of the devices. Furthermore, an ideal blend morphology was obtained for the as-cast QT-DA:PC61BM active layers, thereby eliminating the need for solvent additives or heat treatment.

4. CONCLUSION

In conclusion, this work demonstrates that dicarboxylic acid can be a useful end-functional group in the molecular design of solution-processable conjugated small molecules in improving inter-molecular connectivity and crystallinity. As a proof of concept, we have designed and synthesized donor molecules based on quarterthiophene that contained dicarboxylic acid groups for hydrogen-bonding-induced $\pi-\pi$ interaction. A diester functionalized molecule with the exact same conjugated core is used as a comparison to show the beneficial effects provided by the acid groups at the α- and ω-positions. The −COOH group lead to the formation of a pseudo-polymer, providing a higher propensity to the formation of ordered structures. It was also interesting to note that QT-DA adopted a vertical alignment which provided good charge transportation in the organic solar cell device configuration. Formation of nanofibers and optimal device performance was observed for the as-cast films, thereby reducing the reliance on thermal treatment or solvent additives. The ordered structures resulted in more-efficient devices, compared to the diester-functionalized molecules, which lack the hydrogen-bonding-induced $\pi-\pi$ interaction. It is believed that the use of this interaction will be particularly useful in the enhancement of intermolecular connectivity and crystallinity of molecules with low crystallization ability.

■ ASSOCIATED CONTENT

Supporting Information

The synthetic details and additional characterization data (HRMS, TGA and PESA) for both QT-DA and QT-ES. Weight ratio and layer thickness study for solar cell devices of both QT molecules. XRD patterns for neat films of QT-DA and QT-ES. This material is available free of charge via the Internet at http://pubs.acs.org.

■ AUTHOR INFORMATION

Corresponding Author

*E-mail: ymlam@ntu.edu.sg.

Author Contributions

The manuscript was written through contributions of all authors. All authors have given approval to the final version of the manuscript.

Notes

The authors declare no competing financial interest.

■ ACKNOWLEDGMENTS

K.H.L. acknowledges the schlolarship funding from Ministry of Education, Singapore.

■ REFERENCES

(1) Chen, K.-S.; Salinas, J.-F.; Yip, H.-L.; Huo, L.; Hou, J.; Jen, A. K. Y. *Energy Environ. Sci.* **2012**, *5*, 9551−9557.
(2) Chen, G.; Sasabe, H.; Wang, Z.; Wang, X.-F.; Hong, Z.; Yang, Y.; Kido, J. *Adv. Mater.* **2012**, *24*, 2768−2773.
(3) Li, G.; Shrotriya, V.; Huang, J.; Yao, Y.; Moriarty, T.; Emery, K.; Yang, Y. *Nat. Mater.* **2005**, *4*, 864−868.
(4) Liang, Y. X., Z.; Xia, J.; Tsai, S.-T.; Wu, Y.; Li, G.; Ray, C.; Yu, L. *Adv. Mater.* **2010**, *22*, 1−4.
(5) Peet, J.; Kim, J. Y.; Coates, N. E.; Ma, W. L.; Moses, D.; Heeger, A. J.; Bazan, G. C. *Nat. Mater.* **2007**, *6*, 497−500.
(6) Seo, J. H.; Gutacker, A.; Sun, Y.; Wu, H.; Huang, F.; Cao, Y.; Scherf, U.; Heeger, A. J.; Bazan, G. C. *J. Am. Chem. Soc.* **2011**, *133*, 8416−8419.
(7) Brabec, C. J.; Gowrisanker, S.; Halls, J. J. M.; Laird, D.; Jia, S.; Williams, S. P. *Adv. Mater.* **2010**, *22*, 3839−3856.
(8) Marsh, R. A.; Hodgkiss, J. M.; Albert-Seifried, S.; Friend, R. H. *Nano Lett.* **2010**, *10*, 923−930.
(9) Thompson, B. C.; Fréchet, J. M. J. *Angew. Chem., Int. Ed.* **2008**, *47*, 58−77.
(10) Vanlaeke, P.; Swinnen, A.; Haeldermans, I.; Vanhoyland, G.; Aernouts, T.; Cheyns, D.; Deibel, C.; D'Haen, J.; Heremans, P.; Poortmans, J.; Manca, J. V. *Sol. Energ. Mater. Sol. Cells* **2006**, *90*, 2150−2158.
(11) Yu, G.; Gao, J.; Hummelen, J. C.; Wudl, F.; Heeger, A. J. *Science* **1995**, *270*, 1789−1791.
(12) Li, Z.; He, G.; Wan, X.; Liu, Y.; Zhou, J.; Long, G.; Zuo, Y.; Zhang, M.; Chen, Y. *Adv. Energy Mater.* **2012**, *2*, 74−77.
(13) Loser, S.; Bruns, C. J.; Miyauchi, H.; Ortiz, R. o. P.; Facchetti, A.; Stupp, S. I.; Marks, T. J. *J. Am. Chem. Soc.* **2011**, *133*, 8142−8145.
(14) Sun, Y.; Welch, G. C.; Leong, W. L.; Takacs, C. J.; Bazan, G. C.; Heeger, A. J. *Nat. Mater.* **2012**, *11*, 44−48.
(15) Walker, B.; Kim, C.; Nguyen, T.-Q. *Chem. Mater.* **2010**, *23*, 470−482.
(16) Zhou, J.; Wan, X.; Liu, Y.; Zuo, Y.; Li, Z.; He, G.; Long, G.; Ni, W.; Li, C.; Su, X.; Chen, Y. *J. Am. Chem. Soc.* **2012**, *134*, 16345−16351.
(17) Coffin, R. C.; Peet, J.; Rogers, J.; Bazan, G. C. *Nat. Chem.* **2009**, *1*, 657−661.
(18) Kline, R. J.; McGehee, M. D.; Kadnikova, E. N.; Liu, J.; Fréchet, J. M. J.; Toney, M. F. *Macromolecules* **2005**, *38*, 3312−3319.

(19) Moet, D. J. D.; Lenes, M.; Kotlarski, J. D.; Veenstra, S. C.; Sweelssen, J.; Koetse, M. M.; de Boer, B.; Blom, P. W. M. *Org. Electron.* **2009**, *10*, 1275−1281.
(20) Müller, C.; Wang, E.; Andersson, L. M.; Tvingstedt, K.; Zhou, Y.; Andersson, M. R.; Inganäs, O. *Adv. Funct. Mater.* **2010**, *20*, 2124−2131.
(21) Lee, O. P.; Yiu, A. T.; Beaujuge, P. M.; Woo, C. H.; Holcombe, T. W.; Millstone, J. E.; Douglas, J. D.; Chen, M. S.; Fréchet, J. M. J. *Adv. Mater.* **2011**, *23*, 5359−5363.
(22) Wasserfallen, D.; Fischbach, I.; Chebotareva, N.; Kastler, M.; Pisula, W.; Jäckel, F.; Watson, M. D.; Schnell, I.; Rabe, J. P.; Spiess, H. W.; Müllen, K. *Adv. Funct. Mater.* **2005**, *15*, 1585−1594.
(23) Yu, G.; Zhang, C.; Heeger, A. J. *Appl. Phys. Lett.* **1994**, *64*, 1540−1542.
(24) Malliaras, G. G.; Salem, J. R.; Brock, P. J.; Scott, C. *Phys. Rev. B* **1998**, *58*, R13411−R13414.
(25) Lenes, M.; Morana, M.; Brabec, C. J.; Blom, P. W. M. *Adv. Funct. Mater.* **2009**, *19*, 1106−1111.
(26) Vaidyanathan, S.; Dötz, F.; Katz, H. E.; Lawrentz, U.; Granstrom, J.; Reichmanis, E. *Chem. Mater.* **2007**, *19*, 4676−4681.
(27) Liang, Y.; Feng, D.; Wu, Y.; Tsai, S.-T.; Li, G.; Ray, C.; Yu, L. *J. Am. Chem. Soc.* **2009**, *131*, 7792−7799.
(28) Guo, X.; Zhou, N.; Lou, S. J.; Hennek, J. W.; Ponce Ortiz, R.; Butler, M. R.; Boudreault, P.-L. T.; Strzalka, J.; Morin, P.-O.; Leclerc, M.; López Navarrete, J. T.; Ratner, M. A.; Chen, L. X.; Chang, R. P. H.; Facchetti, A.; Marks, T. J. *J. Am. Chem. Soc.* **2012**, *134*, 18427−18439.
(29) Kemp, W. *Organic Spectroscopy*; W. H. Freeman & Co.: New York, 1991.
(30) SilversteinR.M, *Spectrometric Identification of Organic Compounds*; John Wiley & Sons: New York, 1998.
(31) Gershevitz, O.; Sukenik, C. N. *J. Am. Chem. Soc.* **2003**, *126*, 482−483.
(32) Ma, W.; Yang, C.; Gong, X.; Lee, K.; Heeger, A. J. *Adv. Funct. Mater.* **2005**, *15*, 1617−1622.
(33) Verploegen, E.; Miller, C. E.; Schmidt, K.; Bao, Z.; Toney, M. F. *Chem. Mater.* **2012**, *24*, 3923−3931.
(34) Whitten, D. G. *Acc. Chem. Res.* **1993**, *26*, 502−509.
(35) Shin, W.; Yasuda, T.; Watanabe, G.; Yang, Y. S.; Adachi, C. *Chem. Mater.* **2013**, *25* (12), 2549−2556.
(36) Tuladhar, S. M.; Sims, M.; Choulis, S. A.; Nielsen, C. B.; George, W. N.; Steinke, J. H. G.; Bradley, D. D. C.; Nelson, J. *Org. Electron.* **2009**, *10*, 562−567.
(37) Moulé, A. J.; Meerholz, K. *Adv. Funct. Mater.* **2009**, *19*, 3028−3036.
(38) Wang, T.; Pearson, A. J.; Lidzey, D. G.; Jones, R. A. L. *Adv. Funct. Mater.* **2011**, *21*, 1383−1390.
(39) Walker, B.; Tamayo, A. B.; Dang, X.-D.; Zalar, P.; Seo, J. H.; Garcia, A.; Tantiwiwat, M.; Nguyen, T.-Q. *Adv. Funct. Mater.* **2009**, *19*, 3063−3069.
(40) Wong, W. W. H.; Singh, T. B.; Vak, D.; Pisula, W.; Yan, C.; Feng, X.; Williams, E. L.; Chan, K. L.; Mao, Q.; Jones, D. J.; Ma, C.-Q.; Müllen, K.; Bäuerle, P.; Holmes, A. B. *Adv. Funct. Mater.* **2010**, *20*, 927−938.
(41) Wong, W. W. H.; Ma, C.-Q.; Pisula, W.; Yan, C.; Feng, X.; Jones, D. J.; Müllen, K.; Janssen, R. A. J.; Bäuerle, P.; Holmes, A. B. *Chem. Mater.* **2009**, *22*, 457−466.
(42) Treat, N. D.; Varotto, A.; Takacs, C. J.; Batara, N.; Al-Hashimi, M.; Heeney, M. J.; Heeger, A. J.; Wudl, F.; Hawker, C. J.; Chabinyc, M. L. *J. Am. Chem. Soc.* **2012**, *134*, 15869−15879.
(43) Clarke, T. M.; Durrant, J. R. *Chem. Rev.* **2010**, *110*, 6736−6767.
(44) Jain, A.; Kapoor, A. *Sol. Energy Mater. Sol. Cells* **2005**, *86*, 197−205.
(45) Lee, J. H.; Cho, S.; Roy, A.; Jung, H.-T.; Heeger, A. J. *Appl. Phys. Lett.* **2010**, *96*, 163303.
(46) Koster, L. J. A.; Mihailetchi, V. D.; Blom, P. W. M. *Appl. Phys. Lett.* **2006**, *88*, 052104-1−052104-3.
(47) Wagenpfahl, A.; Rauh, D.; Binder, M.; Deibel, C.; Dyakonov, V. *Phys. Rev. B* **2010**, *82*, 115306.
(48) Burkhard, G. F.; Hoke, E. T.; Scully, S. R.; McGehee, M. D. *Nano Lett.* **2009**, *9*, 4037−4041.
(49) Hoke, E. T.; Vandewal, K.; Bartelt, J. A.; Mateker, W. R.; Douglas, J. D.; Noriega, R.; Graham, K. R.; Fréchet, J. M. J.; Salleo, A.; McGehee, M. D. *Adv. Energy Mater.* **2012**, *3* (2), 220−230 (DOI: 10.1002/aenm.201200474).
(50) Bao, Z.; Lovinger, A. J.; Dodabalapur, A. *Appl. Phys. Lett.* **1996**, *69*, 3066−3068.
(51) See, K. C.; Landis, C.; Sarjeant, A.; Katz, H. E. *Chem. Mater.* **2008**, *20*, 3609−3616.
(52) Sun, Y. M.; Xiao, K.; Liu, Y. Q.; Wang, J. L.; Pei, J.; Yu, G.; Zhu, D. B. *Adv. Funct. Mater.* **2005**, *15*, 818−822.
(53) Yang, C.; Kim, J. Y.; Cho, S.; Lee, J. K.; Heeger, A. J.; Wudl, F. *J. Am. Chem. Soc.* **2008**, *130*, 6444−6450.
(54) Worfolk, B. J.; Rider, D. A.; Elias, A. L.; Thomas, M.; Harris, K. D.; Buriak, J. M. *Adv. Funct. Mater.* **2011**, *21*, 1816−1826.
(55) Jeong, S.-M.; Kim, T.-G.; Jung, E.; Park, J.-W. *ACS Appl. Mater. Interfaces* **2013**, *5*, 6837−6842.
(56) Głowacki, E. D.; Irimia-Vladu, M.; Kaltenbrunner, M.; Gsiorowski, J.; White, M. S.; Monkowius, U.; Romanazzi, G.; Suranna, G. P.; Mastrorilli, P.; Sekitani, T.; Bauer, S.; Someya, T.; Torsi, L.; Sariciftci, N. S. *Adv. Mater.* **2013**, *25*, 1563−1569.
(57) Ball, J. M.; Wöbkenberg, P. H.; Colléaux, F.; Heeney, M.; Anthony, J. E.; McCulloch, I.; Bradley, D. D. C.; Anthopoulos, T. D. *Appl. Phys. Lett.* **2009**, *95*, 103310 (DOI: 10.1063/1.3212736).
(58) Salim, T.; Sun, S.; Wong, L. H.; Xi, L.; Foo, Y. L.; Lam, Y. M. *J. Phys. Chem. C* **2010**, *114*, 9459−9468.
(59) Sun, S.; Salim, T.; Wong, L. H.; Foo, Y. L.; Boey, F.; Lam, Y. M. *J. Mater. Chem.* **2011**, *21*, 377−386.
(60) Berson, S.; De Bettignies, R.; Bailly, S.; Guillerez, S. *Adv. Funct. Mater.* **2007**, *17*, 1377−1384.
(61) Kim, J. S.; Lee, J. H.; Park, J. H.; Shim, C.; Sim, M.; Cho, K. *Adv. Funct. Mater.* **2011**, *21*, 480−486.
(62) Xin, H.; Ren, G.; Kim, F. S.; Jenekhe, S. A. *Chem. Mater.* **2008**, *20*, 6199−6207.
(63) Chen, T.-A.; Wu, X.; Rieke, R. D. *J. Am. Chem. Soc.* **1995**, *117*, 233−244.
(64) Lin, Y.; Lim, J. A.; Wei, Q.; Mannsfeld, S. C. B.; Briseno, A. L.; Watkins, J. J. *Chem. Mater.* **2012**, *24*, 622−632.
(65) Qiu, L.; Wang, X.; Lee, W. H.; Lim, J. A.; Kim, J. S.; Kwak, D.; Cho, K. *Chem. Mater.* **2009**, *21*, 4380−4386.
(66) Sirringhaus, H.; Brown, P. J.; Friend, R. H.; Nielsen, M. M.; Bechgaard, K.; Langeveld-Voss, B. M. W.; Spiering, A. J. H.; Janssen, R. A. J.; Meijer, E. W.; Herwig, P.; de Leeuw, D. M. *Nature* **1999**, *401*, 685−688.
(67) Coakley, K. M.; Srinivasan, B. S.; Ziebarth, J. M.; Goh, C.; Liu, Y.; McGehee, M. D. *Adv. Funct. Mater.* **2005**, *15*, 1927−1932.
(68) Aryal, M.; Trivedi, K.; Hu, W. *ACS Nano* **2009**, *3*, 3085−3090.